

Aeroelastic Design and LPV Modelling of an Experimental Wind Turbine Blade equipped with Free-floating Flaps

S. T. Navalkar¹, L. O. Bernhammer², J. Sodja³, C. J. Slinkman¹,
J. W. van Wingerden¹ and G. A. M. van Kuik²

¹Delft Center for Systems and Control, Delft University of Technology, 2628 CD Delft, the Netherlands

²Wind Energy Group, Delft University of Technology, 2629 HS Delft, the Netherlands

³Aerospace Structures and Computational Mechanics, Delft University of Technology, 2629 HS Delft, the Netherlands

E-mail: s.t.navalkar@tudelft.nl

Abstract. Trailing edge flaps located outboard on wind turbine blades have recently shown considerable potential in the alleviation of turbine lifetime dynamic loads. The concept of the free-floating flap is specifically interesting for wind turbines, on account of its modularity and enhanced control authority. Such a flap is free to rotate about its axis; camberline control of the free-floating flap allows for aeroelastic control of blade loads. This paper describes the design of a scaled wind turbine blade instrumented with free-floating flaps, intended for use in wind tunnel experiments. The nature of the flap introduces a coupled form of flutter due to the aeroelastic coupling of flap rigid-body and blade out-of-plane modes; for maximal control authority it is desired to operate close to the flutter limit. Analytical and numerical methods are used to perform a flutter analysis of the turbine blade. It is shown that the potential flow aeroelastic model can be recast as a continuous-time Linear-Parameter-Varying (LPV) state space model of a low order, for which formal controller design methodologies are readily available.

1. Introduction

The increasing size of modern wind turbines demands that blade load alleviation should be performed at a distributed, local level along the blade span, as with so-called ‘smart’ rotors, which are equipped with local flow-control devices, outlined in [1]. The concept of trailing edge flaps has shown the largest control authority, however, there remain a few challenges that impede its implementation. Firstly, integrated trailing-edge flaps maintenance issues can easily negate the potential cost-savings. Secondly, trailing edge flaps demand high bandwidth actuators with high power-to-weight ratios [2]; such actuators typically have low stroke and hence lowered control authority.

Free-floating flaps, introduced in [3] provide a solution to both these issues. A free-floating flap is essentially a trailing-edge flap that can rotate freely about its axis. A small tab located at its trailing edge provides actuation capabilities. Within the frequency range of interest, the tab deflections lead to magnified flap deflections, thereby increasing the control authority of the flaps. Further, as shown in [4], the flap can be made entirely autonomous, and, as a plug-and-play addition to the wind turbine blade, increases its modularity.



As has already been demonstrated in [4], aeroelastic coupling of the first flexible mode of the blade and the rigid-body flap motion can yield flutter at wind speeds within the operational regime of the wind turbine. While it is imperative to mitigate this unstable phenomenon, the free-floating flaps show the greatest efficiency when operating close to flutter. While a controller operating in closed-loop can stabilise the system, the highly non-linear nature of the aeroelastic system causes a large increase in the conservatism if robust control design principles are followed.

Free-floating flaps have been validated with wind tunnel experiments [4], for wings without twist and taper, and in a non-rotating framework. The objective of the current paper is to design turbine blades with free-floating flaps that can be tested on a scaled wind turbine prototype in the Open Jet Facility wind tunnel at the Delft University of Technology. Further, while it has been numerically concluded that both the flap control authority and the coupling of flap and blade modes varies strongly with the operating wind speed, a model of the system suitable for controller design is not yet available. The second objective of this paper is to derive and validate a linear-parameter-varying (LPV) state-space model of the system of a sufficiently low order such that it can be directly used for both flutter prediction as well as controller design.

2. Blade and Free-Floating Flap (FFF) design

The experimental turbine is a two-bladed machine of diameter 2 m, with a design tip-speed ratio of 3.7. The overall aerodynamic and structural design of the blades follows the procedure described in [5], since the blades were designed for similar wind tunnel testing conditions. As the wind tunnel experiments will also incorporate blade pitch control, the torsional inertia of the blades was reduced by scaling down the root chord by 30%. The root chord thus measures 200 mm, tapering to a tip chord value of 120 mm over a blade length of 750 mm, with a total blade twist of 12°. The blade was 3D printed as a 3 mm-thick shell, with an internal spar structure, using stereolithography techniques, in the material PC-ABS. A spanwise slot was engraved on the top and bottom sides of the blade; this slot was filled with a 0.14 mm thick layer of carbon fibre in a matrix of epoxy resin, to tune the stiffness properties of the blade. The operational speed of the wind turbine is designed to be 230 rpm, yielding an average Reynold's number of approximately 200,000. Since this is lower than the operational speed of the reference turbine [5], which is 370 rpm, the first eigenfrequency of the blade designed was also scaled down. This frequency is designed to be 20 Hz. A CAD model of the blade can be seen in Fig. 1.

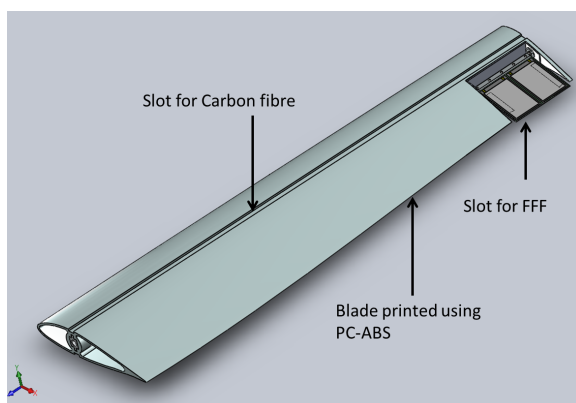


Figure 1. Blade CAD model

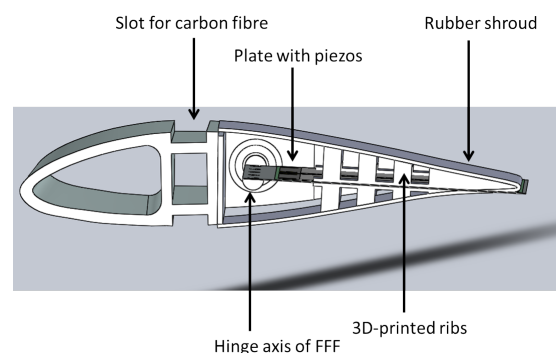


Figure 2. Flap cross-section, chordwise size 120 mm, shell thickness 3 mm. The flap forms 40% of the chord.

The free-floating flap is designed to fit into a slot located at the extreme outboard position. As can be observed in Fig. 2, it is free to rotate about its hinge axis. Two limit stops ensure that

the flap rotation is contained within reasonable limits. The flap consists of a thin metal plate which changes curvature based on the voltage applied to the piezoelectric actuators bonded on the top and bottom surfaces of the plate. In order to ensure that there are no discontinuities in the aerodynamic surface, rubber shrouds are affixed to the blade, supported by 3D printed ribs bonded to the top and bottom of the metal plate.

3. Numerical analysis

The experimental blade is modelled numerically in MSc Nastran [7], version 2004, in order to identify the control-relevant dynamics of the blade. The blade is modelled as a cantilever beam with 1D CBAR elements, connected rigidly with flat-plate aerodynamic panels. The flap is modelled in a similar manner; it is connected to the blade far outboard such that it is able to rotate freely about its axis. The wind speed is taken constant spanwise along the blade; this assumption has limited validity: the wind speed at the blade root will be considerably lower than that at the flap. However, since the blade structural motion close to the root is also significantly smaller, it is expected that this assumption is a good first-order approximation of the aeroelastic behaviour of the model.

The validity of this assumption is at this point unknown, it would be necessary to model the blade numerically in a rotating frame of reference and investigate the change in system dynamics as a function of ambient wind speed. Since Nastran does not afford the possibility to model the blade in this manner, this approach is considered out of scope for the current paper. Further, Nastran does not account for wake effects or inertia forces which will, in practice, alter the aerodynamics of the system. Corrections for these effects would be required to reduce modelling error, however they have not been considered in this section.

A modal analysis is conducted with NASTRAN; the mode shapes and frequencies obtained therefrom are tabulated in Table 1. At zero wind speed, the first structural mode is the rigid body motion of the flap at 0 Hz. A few selected flexible modes of the blade are depicted in Fig. 3 to Fig. 6. The first blade flexible mode is predominantly out-of-plane, and has a frequency of 19.44 Hz, this mode is likely to be excited by wind inflow and forms the most important structural degree of freedom. The blade is considerably stiffer in the lead-lag and torsional degrees of freedom, as evidenced by the higher natural frequencies. Modern wind turbine blades also typically show higher stiffness in these degrees of freedom, and the subsequent modelling and analysis will hence focus purely on the interplay of the rigid-body flap motion and the first flexible out-of-plane blade motion.

Table 1. Structural modes of the blade at zero total air speed

Mode description	Modal frequency	Mode description	Modal frequency
Rigid-body flap mode	0 Hz	1 st Out-of-plane mode	19.44 Hz
1 st In-plane mode	76.67 Hz	2 nd Out-of-plane mode	87.88 Hz
3 rd Out-of-plane mode	223.9 Hz	2 nd In-plane mode	291.3 Hz
1 st Torsional mode	361.6 Hz	4 th Out-of-plane mode	449.6 Hz

A flutter analysis of the blade is conducted next in NASTRAN to understand the change in the blade modes with increasing incident air speed. The air speed values are chosen such that they fall within the range of the effective wind speed experienced by the blade in the experimental setting. In the next section, an analytical LPV model is set up to describe the

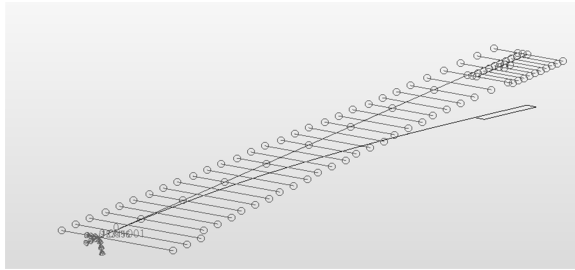


Figure 3. Second mode: First blade out-of-plane, frequency 19.44 Hz

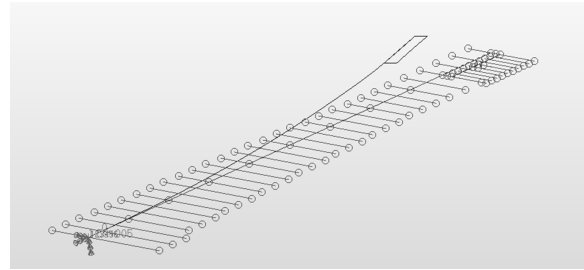


Figure 4. Third mode: First blade in-plane, frequency 76.67 Hz

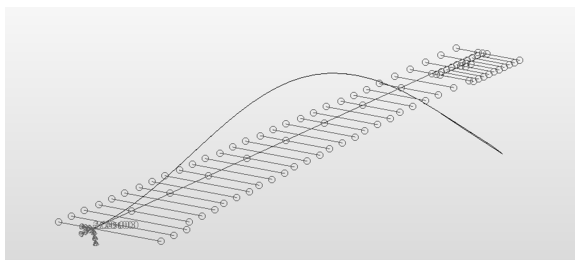


Figure 5. Fourth mode: Second blade out-of-plane, frequency 87.88 Hz

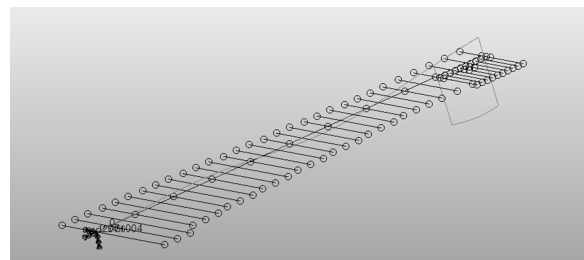


Figure 6. Seventh mode: First blade torsional, frequency 361.6 Hz

system aeroelastic behaviour: this model is also capable of predicting the flutter behaviour of the blade. The numerical and analytical model results are compared in Section 5.

4. Potential-flow LPV modelling and preliminary results

The objective of the paper is to devise an LPV model of the blade that is rich enough to capture the aeroelastic flutter behaviour of the system, while still remaining low-order, in order to facilitate controller design. Such an LPV model can be synthesised by coupling a low-order structural model of the blade with a linear potential flow-based unsteady aerodynamic model.

4.1. Structural model

It should be noted that the scaled turbine blade loads sought to be controlled lie within the frequency range of 0-16 Hz (equivalent to 0P-4P in terms of rotor frequency). From the previous section, it was concluded that the controller-relevant dynamics of the blade can be captured by considering two primary structural degrees of freedom: the first blade out-of-plane mode and rigid-body flap deflection. Additionally, the camberline deformation of the flap provides a control degree of freedom. The structural model can be observed in Fig. 7 and Fig. 8.

From Fig. 7, it can be observed that the blade is modelled as a cantilever constrained to move in the out-of-plane direction. The out of plane motion $Y(s, t)$ as a function of the spanwise coördinate s at time instant t can be decomposed as follows:

$$Y(s, t) = \psi(s)\xi(t), \quad (1)$$

where the spatial mode shape $\psi(s)$ is taken to be the standard first flexural mode shape of a cantilever [8], and is described by:

$$\psi(s) = \cosh(1.8751s/\ell) - \cos(1.8751s/\ell) - 0.7341(\sinh(1.8751s/\ell) - \sin((1.8751s/\ell))), \quad (2)$$

where ℓ is the length of the blade. This description assumes that the blade has homogeneous structural properties in the spanwise direction; this is not strictly true since the chord length reduces along the span of the blade. As seen in the figure, under normal operating conditions, the aerodynamic forces $f(x, t)$ act along the span of the blade.

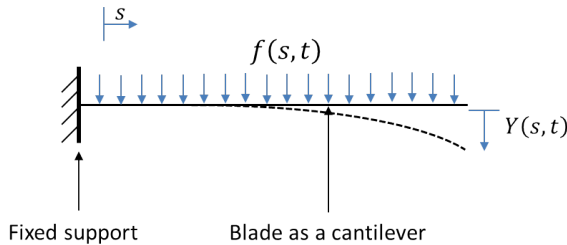


Figure 7. Blade front view: pure out-of-plane motion

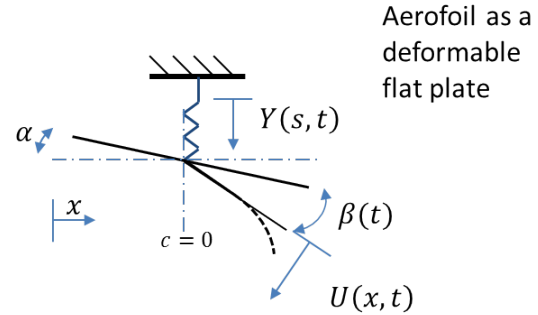


Figure 8. Blade cross-section at flap location

The flap is located between the spanwise stations ℓ_f and ℓ . The blade cross-section at the spanwise location $s \geq \ell_f$ is modelled as shown in Fig. 8. The aerofoil is modelled as a flat plate, with an angle of attack α (equal to the full-span pitch angle of the blade). In principle, this can also be considered to be a control degree of freedom, since modern wind turbine blades are invariably equipped with blade full-span pitch actuators. However, in this analysis, the angle of attack is considered to be fixed over time. Since the blade is optimally twisted to maintain the same angle of attack along blade span, for this spanwise constant wind speed analysis, the twist of the blade is set identically to zero.

The out-of-plane motion $Y(s, t)$ of the blade translates to the heave motion of the aerofoil at location s . Further, the flap is free to move about its hinge axis, which is taken at the chordwise location $c = 0$ from the centre of the aerofoil. The flap rigid-body angular motion is denoted by $\beta(t)$ in the figure, as well as in the sequel. Finally, the flap camberline deformation $U(x, t)$ as a function of chordwise coördinate x forms the control degree of freedom. The camberline is also considered to deform in a manner similar to the first mode of a cantilever, thus the same modal decomposition is used for $U(x, t)$:

$$U(x, t) = \psi(x)u(t). \quad (3)$$

This assumption is not entirely justified, since the connection of the free-floating flap to the hinge can be modelled with greater accuracy as a pin connection than a fully-clamped support. However, the error incurred by considering flap deformation in the cantilever mode is minimal. It should be noted that the term x is rendered dimensionless by normalising it with the corresponding semi-chord $b(s)$. The total camberline deformation y at an arbitrary spanwise location s along the blade is thus described as:

$$y(x, s, t) = \sum_{i=0}^3 y_i(x, s)\phi_i(t), \quad (4)$$

where the terms y_i and ϕ_i are described in Table 2.

With the degrees of freedom defined, it is possible to set up equations of motion for the structural model. The cantilever motion of the beam can be modelled as:

$$M\ddot{\xi}(t) + B\dot{\xi}(t) + K\xi(t) = \Xi(t). \quad (5)$$

Table 2. Camberline deformation terms

Description	Spatial term	Temporal term
Angle of attack	$y_0(x, s) = -\alpha b(s)x$	$\phi_0(t) = 1$
Out-of-plane motion	$y_1(x, s) = \psi(s)$	$\phi_1(t) = \xi(t)$
Flap rigid-body motion	$y_2(x, s) = -b(s)x$ for $s \geq \ell_f, x \geq c$	$\phi_2(t) = \beta(t)$
Control camberline deflection	$y_3(x, s) = \psi(x)b(s)$ for $s \geq \ell_f, x \geq c$	$\phi_3(t) = u(t)$

Here, the terms M , B and K are the generalised mass, damping and stiffness terms associated with the first mode of the cantilever beam. Similarly, the term $\Xi(t)$ is the generalised aerodynamic force associated with this mode. These terms can be obtained using the principle of virtual work as [8]:

$$M = \int_0^\ell m(s)\psi(s)^2 ds, \quad K = \int_0^\ell EI(s)\psi''(s)^2 ds, \quad B = b_\xi K, \quad (6)$$

$$\Xi(t) = \int_0^\ell f(s, t)\psi(s) ds. \quad (7)$$

Here, $m(s)$ is the mass per unit length of the blade, obtained from NASTRAN, while $EI(s)$ are the spanwise-varying stiffness properties of the blade, also taken from NASTRAN. The term b_ξ is the structural damping associated with the first mode of the blade. The motion of the flap is modelled as follows:

$$I\ddot{\beta} + K_\beta\beta = \Xi_m(t). \quad (8)$$

Here, I is the moment of inertia of the flap about its hinge point. The term K_β is the rotational stiffness to flap motion, which is identically zero for a free-floating flap. Finally, the term $\Xi_m(t)$ is the aerodynamic moment around the hinge produced over the flap. The next section describes the model used to arrive at the aerodynamic force $f(s, t)$ and the aerodynamic moment $\Xi_m(t)$ appearing in these equations of motion.

4.2. Aerodynamic model

The aerodynamic modelling of the system follows the procedure laid out in [6], which is valid for describing the sectional dynamics of thin aerofoils of arbitrary camberline geometries, for low angles of attack. This method is a potential-flow method which assumes that the total circulation change is produced by bound vortices distributed along the length of the chord, as well as vortices in the wake of the aerofoil. It should be noted that this model is not directly appropriate for rotor modelling, since it does not consider stall, wake effects and the 3D cross-influence of blade elements. However, it forms a simple first-principles approximation for the behaviour of the free-floating flaps, that can prove useful for controller design.

For an aerofoil with the camberline described by Equation 4, the total aerodynamic force acting per unit span at location s is given by:

$$f(s, t) = \frac{\rho b(s)^2}{\pi} \sum_{i=0}^3 (\ddot{\phi}(t)G_{y,i}(-1) + V\dot{\phi}(t)G_{dyd\epsilon,i}(-1)) + 2\pi\rho b(s)VQ_c(t), \quad (9)$$

where ρ is the density of air. Here, the terms $G_{y,i}$ and $G_{dyd\epsilon,i}$ are geometric and are defined in the following manner:

$$G_{*,i}(c) = \int_c^1 g_{*,i}(x_1) dx, \quad (10)$$

where the functions $g_{*,i}$ are defined as:

$$g_{y,i}(x) = \int_{-1}^1 y_i(x_1) \ln\left(\frac{(x-x_1)^2 + (\sqrt{1-x^2} - \sqrt{1-x_1^2})^2}{(x-x_1)^2 + (\sqrt{1-x^2} + \sqrt{1-x_1^2})^2}\right) dx_1, \quad (11)$$

$$g_{dy\epsilon,i}(x) = \int_{-1}^1 y'_i(x_1) \ln\left(\frac{(x-x_1)^2 + (\sqrt{1-x^2} - \sqrt{1-x_1^2})^2}{(x-x_1)^2 + (\sqrt{1-x^2} + \sqrt{1-x_1^2})^2}\right) dx_1. \quad (12)$$

The expression $y'_i(x)$ refers to the slope of the camberline, thus $\frac{1}{b(s)} \frac{dy_i(x)}{dx}$. The term $Q_c(t)$ in Equation 9 represents the circulatory normal force, and it can be synthesised from a flat plate indicial response in the following manner:

$$Q_c(t) = Q(t)(1 - \tilde{A}_1 - \tilde{A}_2) + z_1(t) + z_2(t) \quad (13)$$

$$Q(t) = -\frac{V}{2\pi} \sum_{i=0}^3 \phi_i(t) H_{dy\epsilon,i} - \frac{1}{2\pi} \dot{\phi}_i(t) H_{y,i}. \quad (14)$$

The terms $H_{*,i}$ are once more geometric and are defined as:

$$H_{y,i} = -2 \int_{-1}^1 \frac{y_i(x) \sqrt{1-x^2}}{x-1} dx, \quad H_{dy\epsilon,i} = -2 \int_{-1}^1 \frac{y'_i(x) \sqrt{1-x^2}}{x-1} dx. \quad (15)$$

The indicial response is empirically fitted using the aerodynamic states $z_*(t)$ which evolve in the following manner:

$$\dot{z}_*(t) + \frac{\tilde{b}_* V z_*}{b(s)} = \frac{\tilde{b}_* \tilde{A}_* V Q(t)}{b(s)}. \quad (16)$$

The empirical coefficients \tilde{A}_* and \tilde{b}_* for a flat plate are obtained from [9].

In a similar manner, the aerodynamic moment over the flap can be obtained as:

$$\Xi_m(t) = \int_{\ell_f}^{\ell} M_p(s) ds, \quad (17)$$

$$\begin{aligned} M_p(s) = & \frac{\rho b(s)^2 V^2}{\pi} \sum_{i=0}^3 \phi_i(t) G_{dy\epsilon,i}(c) + \rho b(s)^2 V^2 \frac{K_1(c)}{2\pi} \sum_{i=0}^3 \phi_i(t) H_{dy\epsilon,i} \\ & - \frac{\rho b(s)^3 V}{\pi} \sum_{i=0}^3 \dot{\phi}_i(t) (I_{dy\epsilon,i}(c) - c G_{dy\epsilon,i}(c)) + \frac{\rho b(s)^2 V}{\pi} \sum_{i=0}^3 \dot{\phi}_i(t) G_{y,i}(c) \\ & + \rho b(s)^2 V \frac{K_1(c)}{2\pi} \sum_{i=0}^3 \dot{\phi}_i H_{y,i} - \frac{\rho b(s)^3}{\pi} \sum_{i=0}^3 \ddot{\phi}_i(t) (I_{y,i}(c) - c G_{y,i}(c)) \\ & + 2\rho b(s)^2 V \left(\left(c + \frac{1}{2}\right) \cos^{-1} c - \left(1 + \frac{c}{2}\right) \sqrt{1-c^2} \right) Q_c(t). \end{aligned}$$

where $K_1(c) = \cos^{-1} c - c\sqrt{1-c^2}$. Here, the geometric terms $I_{*,i}$ are given as:

$$I_{y,i}(c) = \int_c^1 x g_{y,i}(x) dx, \quad I_{dy\epsilon,i}(c) = \int_c^1 x g_{dy\epsilon,i}(x) dx. \quad (18)$$

Herewith, it is possible to completely describe the unsteady aerodynamic forces as a second-order differential equation.

4.3. Coupled aeroelastic model

Combining the aerodynamic forces in the Equations 9 and 17 with the structural model from Equations 5 and 8, the following coupled aeroelastic model is arrived at:

$$\begin{aligned}
 \mathcal{M}_{11}\ddot{\xi}(t) &+ \mathcal{B}_{11}V\dot{\xi}(t) + K\dot{\xi}(t) + \mathcal{M}_{12}\ddot{\beta}(t) + \mathcal{B}_{12}V\dot{\beta}(t) + \mathcal{K}_{12}V^2\beta(t) + Q_1Vz_1(t) + Q_1Vz_2(t) \\
 &= \mathcal{M}_{13}\ddot{u}(t) + \mathcal{B}_{13}V\dot{u}(t) + \mathcal{K}_{13}V^2u(t) + N, \\
 \mathcal{M}_{21}\ddot{\xi}(t) &+ \mathcal{B}_{21}V\dot{\xi}(t) + \mathcal{I}\ddot{\beta}(t) + \mathcal{B}_{22}V\dot{\beta}(t) + \mathcal{K}_{22}V^2\beta(t) + Q_2Vz_1(t) + Q_2Vz_2(t) \\
 &= \mathcal{M}_{23}\ddot{u}(t) + \mathcal{B}_{23}V\dot{u}(t) + \mathcal{K}_{23}V^2u(t), \\
 \mathcal{G}\dot{z}_1(t) &+ \mathcal{B}_{41}V\dot{\xi}(t) + \mathcal{B}_{42}V\dot{\beta}(t) + \mathcal{K}_{42}V\beta(t) + Q_3Vz_1(t) = \mathcal{B}_{43}V\dot{u}(t) + \mathcal{K}_{43}Vu(t), \\
 \mathcal{G}\dot{z}_2(t) &+ \mathcal{B}_{51}V\dot{\xi}(t) + \mathcal{B}_{52}V\dot{\beta}(t) + \mathcal{K}_{52}V\beta(t) + Q_4Vz_1(t) = \mathcal{B}_{53}V\dot{u}(t) + \mathcal{K}_{53}Vu(t).
 \end{aligned}$$

Here, it should be noted that $u(t)$, the deflection of the piezobenders, is taken as the control input. Since the response time of the piezoactuators is a few orders of magnitude faster than the aerodynamic response, the dynamics of the piezobenders are not modelled and it is assumed that the desired flap shape $u(t)$ can be instantaneously commanded by the controller.

The coefficients in the above equations are constant and depend purely on the physical and geometric characteristics of the blade. The dependence of the dynamics on the wind speed can be clearly seen in the above differential equations. For the special case where the flap length is exactly half of the chord length ($c = 0$), the coefficients are tabulated in Table 3 with $\bar{A} = 1 - \bar{A}_1 - \bar{A}_2$.

Table 3. Aeroelastic model coefficients

$\mathcal{M}_{11} = M + \pi\rho \int_0^\ell b(s)^2\psi(s)^2ds$	$\mathcal{M}_{12} = -\frac{2}{3}\rho \int_{\ell_f}^\ell b(s)^3\psi(s)ds$
$\mathcal{M}_{21} = -\frac{2}{3}\rho \int_{\ell_f}^\ell b(s)^3\psi(s)ds$	$\mathcal{I} = I + 0.2573\rho \int_{\ell_f}^\ell b(s)^4ds$
$\mathcal{M}_{13} = -0.9629\rho \int_{\ell_f}^\ell b(s)^3\psi(s)ds$	$\mathcal{M}_{23} = 0.3988\rho \int_{\ell_f}^\ell b(s)^4ds$
$\mathcal{B}_{11} = 2\pi\rho\bar{A} \int_0^\ell b(s)\psi(s)^2ds$	$\mathcal{B}_{12} = (1.571 + 3.571\bar{A})\rho \int_{\ell_f}^\ell b(s)^2\psi(s)ds$
$\mathcal{B}_{21} = -0.4292\rho\bar{A} \int_{\ell_f}^\ell b(s)^2\psi(s)ds$	$\mathcal{B}_{22} = (0.8929 + 0.2439\bar{A})\rho \int_{\ell_f}^\ell b(s)^3ds$
$\mathcal{B}_{13} = -(2.878 + 6.346\bar{A})\rho\bar{A} \int_{\ell_f}^\ell b(s)^2\psi(s)ds$	$\mathcal{B}_{23} = (1.896 + 0.4335\bar{A})\rho \int_{\ell_f}^\ell b(s)^3ds$
$\mathcal{B}_{41} = \tilde{b}_1\tilde{A}_1 \int_0^\ell \psi(s)ds$	$\mathcal{B}_{42} = -0.5683\tilde{b}_1\tilde{A}_1 \int_{\ell_f}^\ell b(s)\psi(s)ds$
$\mathcal{B}_{51} = \tilde{b}_2\tilde{A}_2 \int_0^\ell \psi(s)ds$	$\mathcal{B}_{52} = -0.5683\tilde{b}_2\tilde{A}_2 \int_{\ell_f}^\ell b(s)\psi(s)ds$
$\mathcal{B}_{43} = -1.945\tilde{b}_1\tilde{A}_1 \int_{\ell_f}^\ell b(s)\psi(s)ds$	$\mathcal{B}_{53} = -1.945\tilde{b}_2\tilde{A}_2 \int_{\ell_f}^\ell b(s)\psi(s)ds$
$\mathcal{K}_{12} = -5.142\rho\bar{A} \int_{\ell_f}^\ell b(s)\psi(s)ds$	$\mathcal{K}_{13} = -12.22\rho\bar{A} \int_{\ell_f}^\ell b(s)\psi(s)ds$
$\mathcal{K}_{22} = (0.182 + 0.3513\bar{A})\rho \int_{\ell_f}^\ell b(s)^2ds$	$\mathcal{K}_{23} = -(0.931 + 0.8348\bar{A})\rho \int_{\ell_f}^\ell b(s)^2ds$
$\mathcal{K}_{42} = -0.8183\tilde{b}_1\tilde{A}_1(\ell_f - \ell)$	$\mathcal{K}_{43} = -1.01\tilde{b}_1\tilde{A}_1(\ell_f - \ell)$
$\mathcal{K}_{52} = -0.8183\tilde{b}_2\tilde{A}_2(\ell_f - \ell)$	$\mathcal{K}_{53} = -1.01\tilde{b}_2\tilde{A}_2(\ell_f - \ell)$
$Q_1 = -2\pi \int_0^\ell b(s)\psi(s)ds$	$Q_2 = -0.4292\rho \int_{\ell_f}^\ell b(s)^2ds$
$Q_3 = \tilde{b}_1\ell$	$Q_4 = \tilde{b}_2\ell$
$\mathcal{G} = \int_0^\ell b(s)ds$	

The next section compares the flutter analysis from NASTRAN and the potential flow-based LPV model.

5. Results

The experimental blade described in Section 2 was modelled numerically and analytically, as described in Sections 3 and 4 respectively. A flutter analysis was conducted using both modelling techniques, and the resulting flutter diagram can be observed in Fig. 9 and Fig. 10. It can be seen that the frequency of the rigid-body flexible mode, as predicted by both models, increases with increasing incident air speed, starting from 0 Hz in still air. On the other hand, the frequency of the flexible out-of-plane blade mode remains more or less constant over a range of wind speeds.

Both the numerical and analytical models agree well in terms of the prediction of frequency variation. On the other hand, the prediction of the variation of damping with wind speed differs to some extent across the two models. Specifically, the change in damping over wind speed predicted by NASTRAN is higher than that obtained from the potential flow model. The NASTRAN model predicts that the flexible out-of-plane mode becomes unstable at a flutter speed of 33 m/s. On the other hand, flutter does not occur within the investigated wind speeds in the analytical model. Since it was experimentally observed [10] that flutter does indeed occur at a total air speed of around 30 m/s [operating rotor speed 230 rpm], it can be inferred that the NASTRAN model is more accurate than the analytical potential-flow model.

A comparison of the NASTRAN and potential-flow model shows that the cross-coupling of the mass matrices is underpredicted by the potential-flow model. Since the objective of the modelling of the previous section is to arrive at a high-fidelity low-order model suitable for controller synthesis, the off-diagonal matrix elements \mathcal{M}_{12} and \mathcal{M}_{21} are corrected with a factor $K_{cc} = 8$ in order to achieve the appropriate experimentally-observed flutter speed:

$$\mathcal{M}_{12} = \mathcal{M}_{21} = -\frac{2K_{cc}}{3}\rho \int_{\ell_f}^{\ell} b(s)^3 \psi(s) ds. \quad (19)$$

The analytical approach makes the assumption of independence of blade elements, and does not consider the cross-influence of the bound vortices on its spanwise neighbours. As such, when compared to the fully 3D numerical model, it underestimates the cross-coupling effect of the aerodynamic forces. This coupling effect has been corrected for artificially by empirically augmenting the off-diagonal mass terms by using the tuned parameter K_{cc} . Such a parameter can, instead, also be tuned for increasing the off-diagonal stiffness or damping terms. Greater modelling detail is thus demanded by the analytical approach in order to match the fidelity of the numerical approach, in order to relax the assumption of independence of blade elements.

With this correction, the predicted flutter behaviour is remarkably close to the behaviour predicted numerically by NASTRAN. This corrected behaviour is depicted using the dotted line in Fig. 10.

The transfer functions between the control degree of freedom $u(t)$ to the structural degrees of freedom ξ and β are depicted using Bode diagrams in Fig. 11 and Fig. 12. As also seen from the flutter diagram, the frequency of the heavily-damped rigid-body flap motion increases with increasing wind speed. On the other hand, the frequency of the flexible out-of-plane blade motion remains almost constant, while the damping transitions from stable to unstable beyond the flutter speed of 35 m/s.

An alternative approach to using a fully free-floating flap is to constrain the rigid-body motion of the flap using a rotational spring. This can be modelled as in Section 4, taking K_β in Equation 17 as a finite non-zero quantity. The aeroelastic behaviour of such an active-passive combination of trailing edge flaps lies halfway between that of a fully free-floating flap $K_\beta = 0$ and a conventional trailing-edge flap $K_\beta = \infty$. The transfer function for a flap equipped with a rotational spring is given in Fig. 13. For low values of spring stiffness, high control authority is obtained at the blade out-of-plane eigenmode, while the control authority reduces for a conventional flap with high stiffness. It is interesting to note that there is an intermediate value of K_β for which low-frequency control authority is substantially higher than for either the

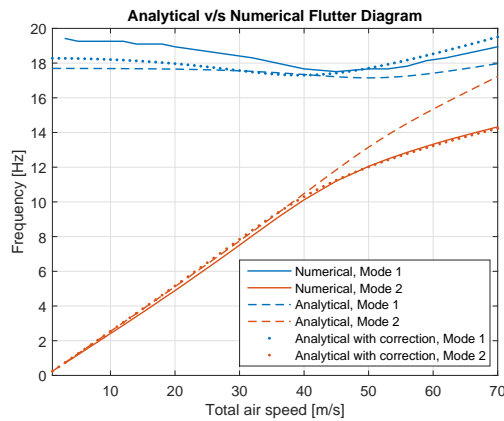


Figure 9. Flutter diagram of blade: Frequency

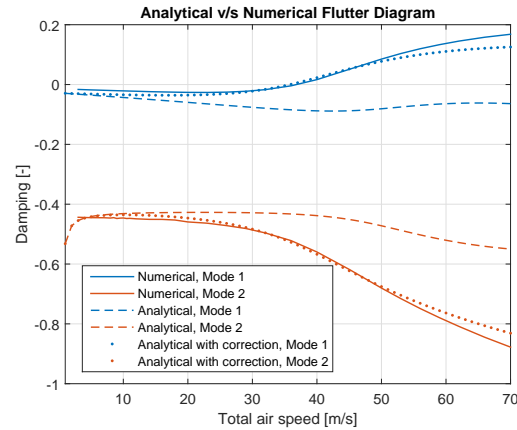


Figure 10. Flutter diagram of blade: Damping

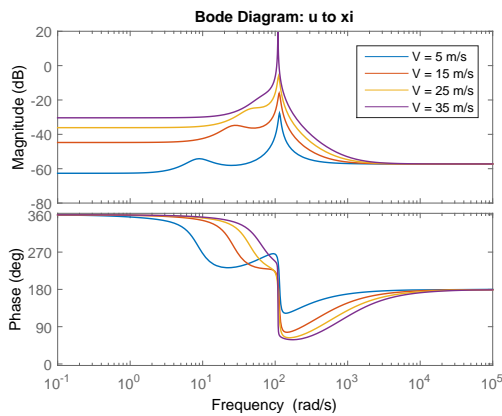


Figure 11. Transfer function from control input to blade out-of-plane motion

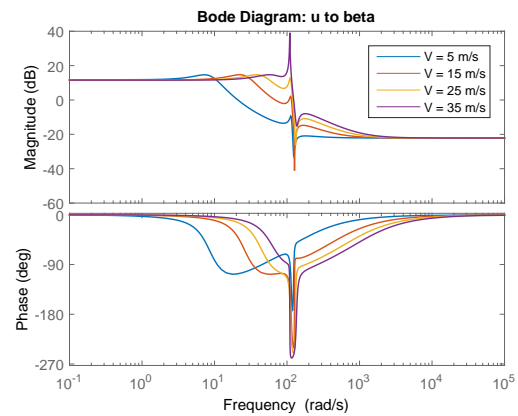


Figure 12. Transfer function from control input to flap rigid motion

free-floating or the conventional trailing-edge flap. The same result can be seen in Fig. 14. For an intermediate value of K_β , as the blade structure becomes more responsive to the flap, the flutter speed reduces. At very high stiffness, the configuration approaches the dynamic behaviour of a conventional flap, and flutter does not occur within the operational envelope.

6. Conclusion

A numerical and analytical model were evaluated for describing the aeroelastic behaviour of an experimental wind turbine blade equipped with a free-floating flap. The flexible blade out-of-plane mode, which dominates the load spectrum of wind turbine blades, couples strongly with the rigid-body motion of the flap. This coupling enhances flap control authority but also produces low-speed flutter that requires addressal.

It is observed that the potential flow-based analytical model underpredicts the off-diagonal aerodynamic mass terms as compared to the numerical model. When a correction factor is applied to increase the cross-coupling of the mass terms, the aeroelastic behaviour predicted by both the numerical and analytical models is remarkably close. With the low-order LPV model derived from the potential flow model, it is now possible to design an LPV controller for the

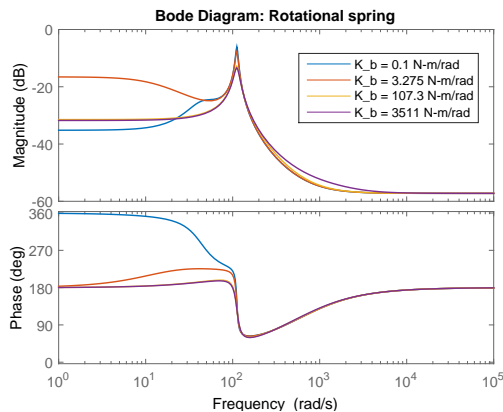


Figure 13. Transfer function from control input to blade out-of-plane motion, flap with rotational spring, total air speed 25 m/s

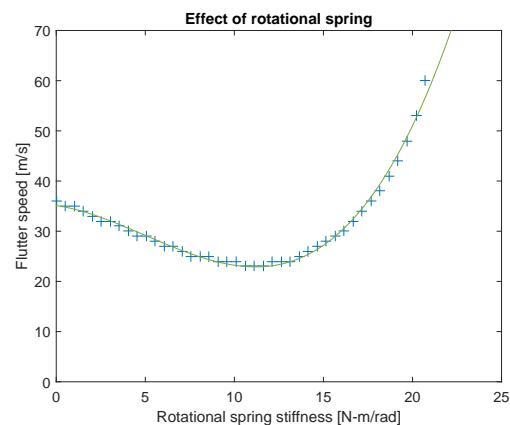


Figure 14. Effect of rotational spring on flutter speed

system, and to stabilise it while maximising load alleviation.

By constraining the motion of the flap with a rotational spring, it is possible to achieve flap aeroelastic behaviour that is intermediate between that of a free-floating flap and a conventional trailing-edge flap. Tuning the spring stiffness (or apposite control design) affords the possibility to achieve the desired trade-off between control authority and flutter avoidance.

References

- [1] ‘Review of the state of the art in smart rotor control for wind turbines’. T. K. Barlas and G. A. M. van Kuik. Progress in Aerospace Sciences, Volume 46, Issue 1, 2010, Pages 1-27.
- [2] ‘A comparison of smart rotor control approaches using trailing edge flaps and individual pitch control’. M. A. Lackner and G. A. M. van Kuik. AIAA Aerospace Sciences Meeting including the New Horizons Forum, 2009, Orlando, USA.
- [3] ‘Aeroelastic control using distributed floating flaps activated by piezoelectric tabs’. L. O. Bernhammer, R. de Breuker, M. Karpel and G. J. van der Veen. Journal of Aircraft, 50(3), 732-740.
- [4] ‘Design of an autonomous flap for load alleviation’. L. O. Bernhammer, J. Sodja, M. Karpel and R. de Breuker. 25th International Conference on Adaptive Structures and Technologies, the Hague, the Netherlands, 2014.
- [5] ‘Two-degree of freedom active vibration control of a prototyped “smart” rotor’. J. W. van Wingerden, A. Hulskamp, T. K. Barlas, I. Houtzager, H. E. N. Bersee, G. A. M. van Kuik and M. Verhaegen. IEEE Transactions on Control Systems Technology, 2010, Pages 284-296.
- [6] ‘Unsteady two-dimensional potential-flow model for thin variable geometry aerofoils’. M. Gaunaa. Wind Energy, Volume 13, 2010, Pages 167-192.
- [7] ‘MSC Nastran aeroelastic analysis user’s guide’. W. Rodden and E. Johnson. MSC Software Corp., Santa Ana, USA, 1994.
- [8] ‘Introduction to structural dynamics and aeroelasticity’. D. H. Hodges and G. A. Pierce. Cambridge University Press, 2011.
- [9] ‘The unsteady lift of a wing of finite aspect ratio’. R. T. Jones. NACA Report 0681, Langley Memorial Aeronautical Laboratory, 1939.
- [10] ‘Wind tunnel tests with combined pitch and free-floating flap control: data-driven iterative feedforward tuning’. S. T. Navalkar, L. O. Bernhammer, J. Sodja, G. A. M. van Kuik and J. W. van Wingerden. Wind Energy Science, under review, 2016.